CrossMark

ORIGINAL PAPER

Structural, optical, photocatalytic, and antimicrobial activities of cobalt-doped tin oxide nanoparticles

Dhanya Chandran[1] · Lakshmi S. Nair[1] · S. Balachandran[2] · K. Rajendra Babu[1,3] · M. Deepa[4]

Abstract In this study, pure and Co-doped tin oxide (SnO_2) nanoparticles were synthesized by sol–gel method, and the effect of Co-doping on the structural, optical, photocatalytic, and antimicrobial activities was studied. The prepared samples were characterized by X-ray diffraction (XRD), high-resolution transmission electron microscopy, energy-dispersive X-ray spectroscopy, UV–visible diffuse reflectance spectroscopy, and N_2 adsorption/desorption analysis. The XRD patterns of all the samples are identified as tetragonal rutile-type SnO_2 phase which is further confirmed by TEM analysis. The optical spectra showed redshift in the absorption edge of doped samples, which enhances their absorption toward the visible light region. The photocatalytic activity of all the samples was assessed by monitoring the degradation of methylene blue solution under daylight illumination, and it was found that the photocatalytic activity significantly increases with the increase in dopant concentration, which is due to the effective charge separation of photogenerated electron–hole pairs. The antimicrobial studies investigated against standard bacterial and fungal strains showed enhanced antimicrobial activity in doped samples, which can be attributed to the production of reactive oxygen species and large surface area of the nanoparticles.

Graphical abstract
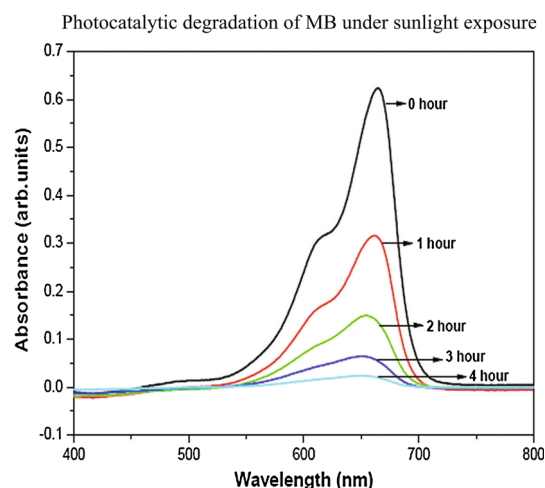
Photocatalytic degradation of MB under sunlight exposure

1 Introduction

Tin oxide is an *n*-type semiconductor with a wide band gap of 3.6 eV and has been used in a large range of technological applications due to its tailor-made properties. It is particularly interesting because of its unique optical, electrical, and catalytic properties and has a wide range of applications mainly gas sensors, optoelectronic devices, lithium-ion batteries, photocatalysis, and dye-sensitized solar cells [1–7]. Recently, SnO_2 has become of much interest in the area of

✉ S. Balachandran
sbcnair@gmail.com

1 Department of Physics, Mahatma Gandhi College, Kerala University, Pattom Palace P. O, Thiruvananthapuram 695004, India

2 Department of Chemistry, Mahatma Gandhi College, Kerala University, Pattom Palace P. O, Thiruvananthapuram 695004, India

3 Heera College of Engineering and Technology, Panavoor P. O, Nedumangadu, Thiruvananthapuram 695568, India

4 Department of Physics, All Saints' College, Kerala University, Chackai P. O, Thiruvananthapuram 695007, India

photocatalysis due to its high photochemical stability, strong oxidizing power, low-cost, and non-toxic nature. Casados et al. [4] show that pure tin oxide has photocatalytic properties similar to that of commercial titanium oxide (Degussa P25) under UV light irradiation in the degradation of methylene blue (MB) for reaction times in the range 0–1 h. However, due to the large band gap observed for SnO_2, it can be photoactivated only by UV irradiation which constitutes only 4–5 % of the entire solar energy, leaving most of the visible portion of solar radiation. This limitation can be overcome by doping SnO_2 with transition metal ions such as Co, Ni, and Mn that extends the absorption spectrum from UV to visible regions, and therefore, the solar energy could be used effectively [8, 9]. In addition to photocatalytic activity, inorganic metal oxides such as TiO_2, ZnO, and SnO_2 doped with transition metal ions have received increasing attention in antimicrobial applications because such materials can achieve effective disinfection without the formation of any harmful by-products [10–14].

There are several methods for the synthesis of SnO_2 nanoparticles such as sol–gel method, solvothermal method, thermal decomposition method, and hydrothermal route. [15–19]. Among them, sol–gel method offers several advantages over other methods such as high purity, better homogeneity, phase-pure powders at a lower temperature, ability to control the grain size, and capability in controlling the textural and surface properties of metal oxides. In this article, pure and Co-doped SnO_2 nanoparticles have been prepared through sol–gel method, and their application toward the photocatalytic degradation of MB under daylight illumination was investigated. The antimicrobial effect of the prepared samples on standard bacterial and fungal strains was also investigated. To the best of our knowledge, very less work has been reported in the antimicrobial properties and photocatalytic activity (under sunlight) of Co-doped SnO_2 nanoparticles.

2 Experimental

2.1 Materials

The chemicals used in this study were $SnCl_4 \cdot 5H_2O$ (Sigma-Aldrich), NH_4OH (25 %, Merck), $Co(Cl)_2 \cdot 6H_2O$ (Merck), methylene blue (Merck). All reagents were used as received without any further purification, and double distilled water was used throughout the experiments.

2.2 Synthesis of pure and Co-doped SnO_2 nanoparticles

Pure and Co-doped tin oxide (SnO_2) nanoparticles have been prepared by sol–gel method with different

concentrations of cobalt (0.75, 3, and 4 at%). In a typical synthesis, 5.8 g of tin (IV) chloride was dissolved in 100 ml ultrapure water and stirred for half an hour. To this solution, 3.2 M ammonia solution was added drop wise under a controlled feed rate of 0.5 ml per min with constant stirring until pH 2 was reached. The sol was then kept at room temperature for 1 day to complete the aging process. The resultant gel was washed several times with ethanol and double distilled water and dried in an oven at 80 °C for 24 h. After grinding, the synthesized powder was calcined at 400 °C for 2 h. Co-doped SnO_2 nanopowders were prepared in a similar manner, by the addition of calculated amount of $Co(Cl)_2 \cdot 6H_2O$ into $SnCl_4 \cdot 5H_2O$ solution.

2.3 Photocatalytic measurements

The photocatalytic activity of the samples was determined by the photodecomposition of MB under sunlight. The whole experiments were carried out on a hot sunny day. The decolorization of MB is taken as a model reaction for evaluating the photocatalytic activity of all the samples. In a typical experiment, 50 mg of photocatalyst is added to 100 ml of 10 μmol MB solution, and the solution is sonicated for 10 min by ultrasonic vibration. Prior to irradiation, the suspension is kept in the dark for 30 min under continuous stirring to establish an adsorption/desorption equilibrium between the photocatalyst and the dye. The solution is then kept under sunlight with constant stirring, and sampling was done at regular time intervals (1 h), centrifuged at 5000 rpm to remove any catalyst particles. The change in MB concentration with irradiation time was determined from their characteristic absorption (λ_{max}) at 665 nm with a UV–visible spectrophotometer. The efficiency of the photocatalysts in the photodegradation of MB under sunlight exposure was calculated using the formula:

$$\%D = {(C - C_0)}/{C_0} \times 100$$

where C_0 is the initial concentration of MB solution and C its concentration at different intervals of irradiation time.

2.4 Antibacterial activity

The antibacterial activity of pure and Co-doped tin oxide nanoparticles was determined using agar-well diffusion method and screened against different Gram-positive bacteria (*Enterococcus faecalis*, *Staphylococcus aureus*) and Gram-negative bacteria (*Escherichia coli*, *Enterobacter* spp., *Pseudomonas aeruginosa*). Mueller-Hinton agar (MHA) plates were swabbed with inoculums of test organisms grown to turbidity equal to 0.5 McFarland scale. After swabbing, agar wells of approximately 10 mm was bored using a well cutter, and the wells in each plate were

loaded with different concentrations (25, 50, 100 µg) of pure and Co-doped tin oxide nanoparticles. The inoculated plates were then incubated at 37 °C for 24 h. The antibacterial activity was assayed by measuring the diameter of the inhibition zone (mm) formed around the well. The larger the zone of inhibition (ZOI) around the well, the greater the antimicrobial activity of the sample will be. Gentamicin was used as the positive control against all the bacteria to compare the efficacy of the test samples.

2.5 Antifungal activity

Aspergillus niger and Candida albicans were employed for testing the antifungal activity of pure and Co-doped tin oxide nanoparticles using agar-well diffusion method. Potato dextrose agar (PDA) plates were prepared, and fungal spores/cells were swabbed. Wells (10 mm) were bored, and samples of different concentrations (25, 50, 100 µg/ml) were added. The ZOI was measured after 3 days and 24-h incubation for Aspergillus niger and Candida albicans, respectively, and compared with the standard antifungal drug, Clotrimazole.

## 3 Characterization and measurements

The X-ray diffraction patterns were recorded with Bruker Advance diffractometer using CuKα ($\lambda = 1.5406$ Å) radiation in 2θ ranging from 20° to 80° at a scanning rate of 0.02 s^{-1}. The morphology, particle size, and structure of the synthesized samples were observed under a transmission electron microscope using JEOL-JEM2100. The compositional analysis of the doped samples was determined from energy-dispersive X-ray spectroscopy (EDAX) spectra using Horiba EMAX. The specific surface area of pure and doped samples was determined from the adsorption isotherm of nitrogen at 77 K on the basis of the Brunauer–Emmett–Teller (BET) method using a micrometrics Gemini 2375, after degassing the samples at 200 °C for 2 h. The UV–visible diffuse reflectance measurements were recorded at room temperature using PerkinElmer Lambda 35 spectrophotometer over a range of 200–800 nm.

4 Results and discussion

4.1 Characterization of the photocatalysts

Figure 1 shows the XRD patterns of pure (CT0), 0.75 at% Co-doped (CT1), 3 at% Co-doped (CT2), and 4 at% Co-doped (CT3) tin oxide nanoparticles calcined at 400 °C synthesized by the sol–gel method. All the diffraction peaks can be indexed to the tetragonal rutile-type SnO$_2$ phase, and
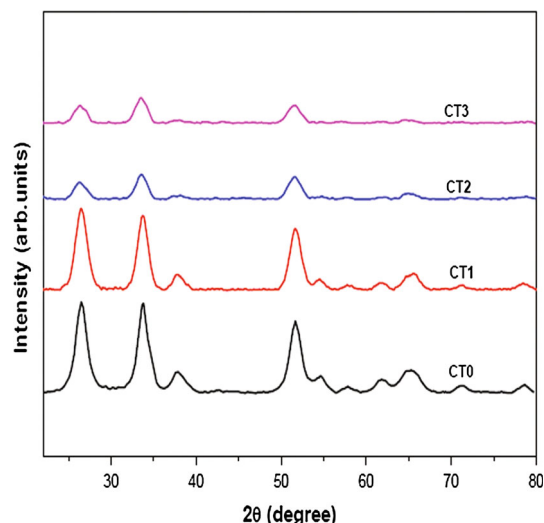
Fig. 1 XRD patterns of pure and Co-doped SnO$_2$ nanoparticles

the results are in good agreement with the standard JCPDS (Card No. 41-1445) data. Further, no characteristic peaks of impurities such as cobalt oxides or other tin oxides were observed in the XRD pattern showing the single phase sample formation. The average crystallite size (*d*) of the sample was estimated using Scherrer's equation [20]:

$$d = 0.9\lambda/\beta\cos\theta$$

where λ is the wavelength of the X-ray used, θ is the Bragg's angle, and β is the full width at half maximum (FWHM) of the peak. The average crystallite size of the samples and the deviation, which is the standard deviation between the sizes estimated along the three different crystallographic directions, are given in Table 1. As compared to pure SnO$_2$, broadening of diffraction peaks and degradation of crystallinity can be observed with increase in cobalt content, which implies the reduction in crystallite size [10, 21–24]. Table 1 shows the lattice parameters of pure and Co-doped SnO$_2$ nanoparticles. The increase in lattice parameters with increase in cobalt concentration shows that Co ions systematically substituted Sn ions in the samples as the ionic radius of Co^{2+} ($r = 0.75$ Å) is larger than that of Sn^{4+} ($r = 0.69$ Å) [8, 25].

Figure 2a provides the TEM image of sample CT3 and the particle size distribution with log-normal profile and selected area diffraction (SAED) patterns in its inset, and Fig. 2b shows the corresponding high-resolution transmission electron microscopy (HRTEM) image. TEM image shows nearly spherical-shaped particles, and average particle size obtained from TEM analysis for all the samples is depicted in Table 1. From the TEM image, the average particle size and the size distribution were estimated by log-normal curve fitting to the observed histograms. It can be observed that the size of nanoparticles obtained from the

Table 1 Comparison of particle size, lattice parameters, band gap energy, rate constant, and photocatalytic degradation efficiency of pure and Co-doped SnO_2 nanoparticles

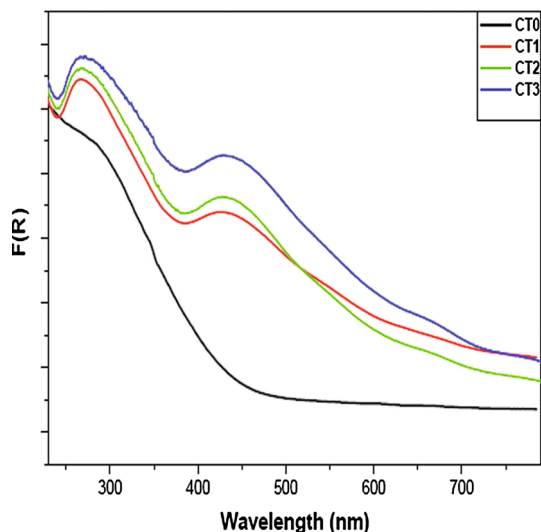| Samples	Size from Scherrer equation (nm)	Lattice parameter a (nm)	Lattice parameter c (nm)	Size from TEM analysis (nm)	Specific surface area (S_{BET}) (m²/g)	Band gap (eV)	Rate constant k (h⁻¹)	%D at $t = 4$ h
CT0	6.97 ± 0.62	4.7403	3.1993	7.63 ± 0.70	67	3.34	0.098	33.1
CT1	5.77 ± 0.18	4.7591	3.1996	5.78 ± 0.69	97	3.10	0.525	88.7
CT2	5.13 ± 0.34	4.7821	3.2126	5.15 ± 0.60	100	3.05	0.593	92.0
CT3	4.93 ± 0.23	4.7821	3.2254	4.97 ± 0.66	130	2.90	0.826	97.0
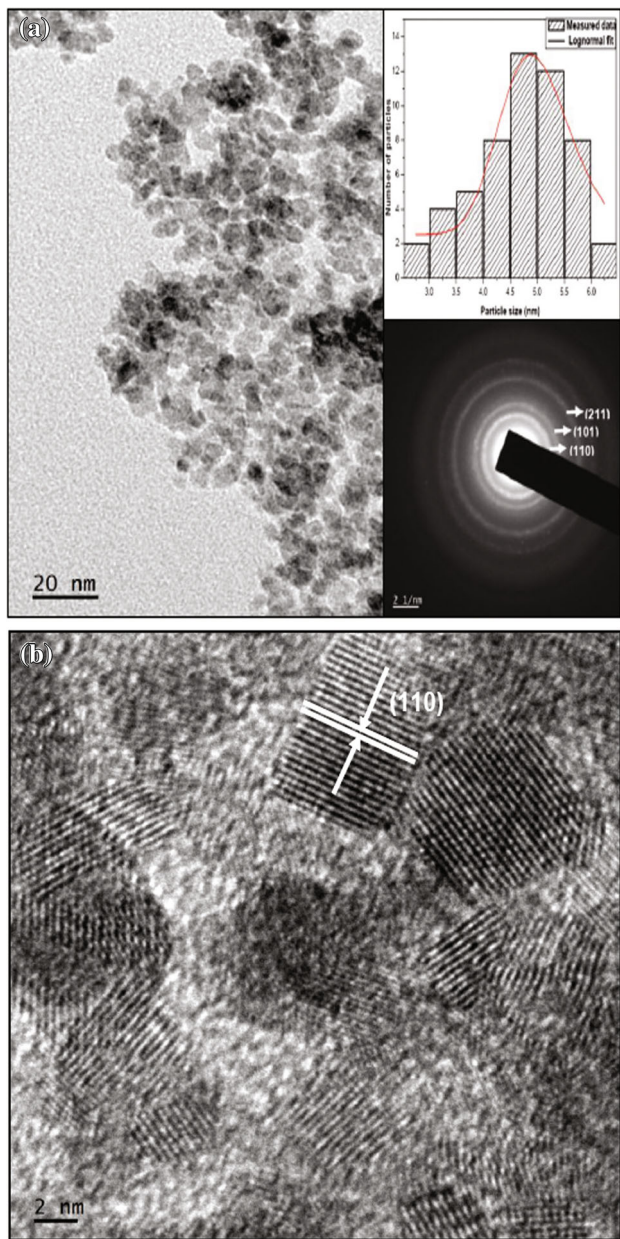
Fig. 2 **a** TEM image of sample CT3, inset showing the particle size distribution with log-normal profile and SAED patterns, **b** HRTEM image of sample CT3
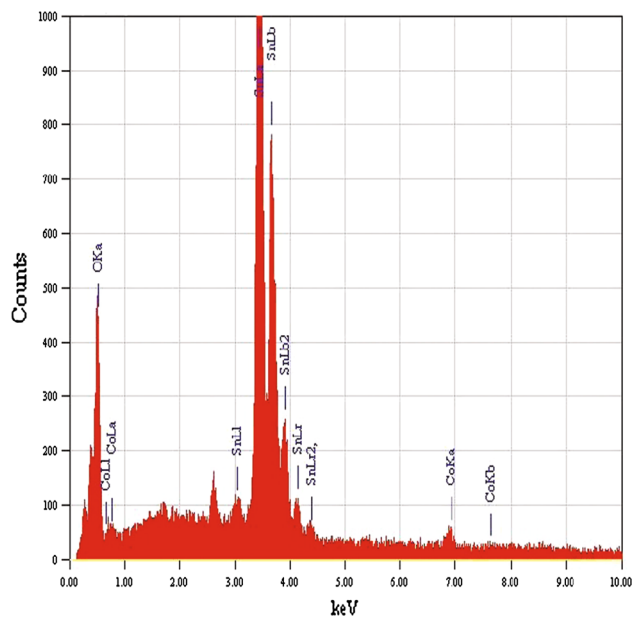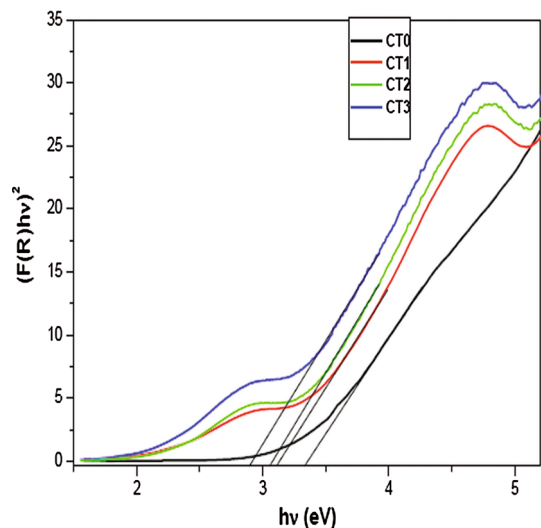

Fig. 3 EDAX spectrum of sample CT3
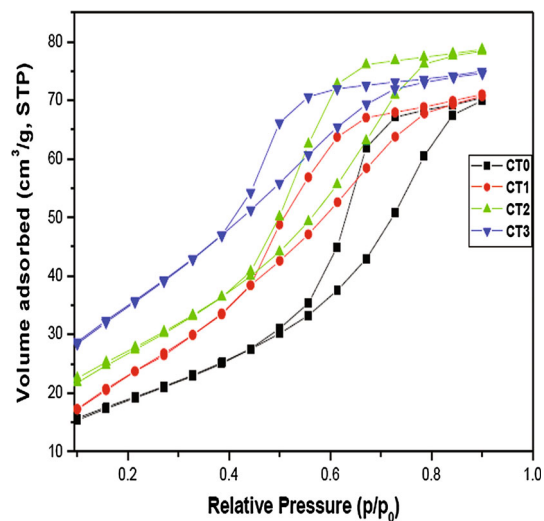
Fig. 4 Nitrogen adsorption/desorption isotherms of pure and Co-doped SnO_2 nanoparticles

Fig. 5 UV–visible spectra of pure and Co-doped SnO_2 nanoparticles

Fig. 7 UV–visible absorption spectra showing the degradation of MB at different time intervals of sunlight exposure using sample CT3
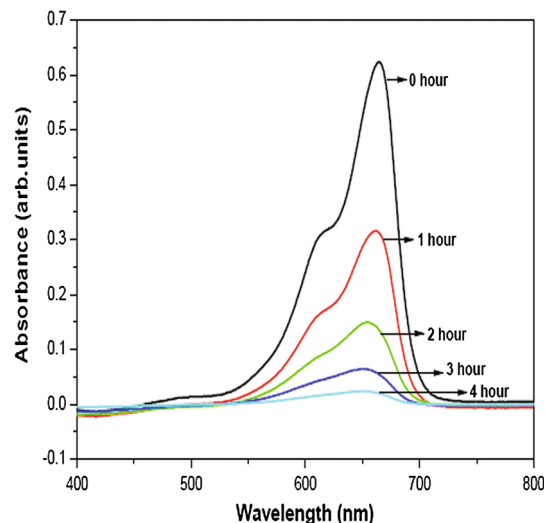

Fig. 6 Band gap energy of pure and Co-doped SnO_2 nanoparticles

TEM images is in close agreement with those obtained from XRD patterns. The SAED patterns exhibited the polycrystalline rings, which could be well indexed to diffractions from the (110), (101), and (211) planes which well characterize the tetragonal SnO_2 structure. HRTEM image clearly reveals the interplanar spacing of 0.34 nm, which corresponds to the (110) crystallographic planes of SnO_2. Hence, the interplanar distances measured from HRTEM image agree well with the data obtained from XRD pattern.

Figure 3 shows the EDAX spectrum of sample CT3 which confirms the existence of Co^{2+} ions in doped samples. Thus, the successful doping of Co^{2+} ions in SnO_2 is confirmed from EDAX and XRD analyses.

Figure 4 shows the N_2 adsorption/desorption isotherms of pure and Co-doped SnO_2 nanoparticles. They exhibit type IV isotherms with a H2-type hysteresis loop observed in the relative pressure (p/p_0) range of 0.45–0.95, revealing the characteristic of mesoporous materials. The specific surface areas of the prepared samples were calculated using the BET method and are given in Table 1, and it was found that the specific surface area increases with increase in Co content.

Figure 5 shows the UV–visible DRS of pure and Co-doped samples. The optical absorption was recorded as the Kubelka–Munk function $F(R) = (1 - R)^2/2R$, where R is the reflectance and $F(R)$ is the absorbance [26]. It can be clearly observed that as the doping percentage of cobalt increases, the absorption edge positions shift toward longer wavelength or lower energies. As compared to pure SnO_2, the doped samples exhibit an extra peak between 375 and 505 nm. Biswajit et al. [27] reported similar peak in Co-doped TiO_2 nanoparticles, and they related this region to the crystal field splitted d-electronic transition of Co^{2+} in octahedral or pseudo-octahedral coordination and ascribed to $^4T_{1g}$–$^4T_{1g}(P)$ transition.

Figure 6 shows the optical band gap (E_g) of the samples determined by extrapolating the linear portion of $[F(R)hv]^2$ versus the photon energy (hv) curve (Tauc plot), to zero absorption. The band gaps determined are summarized in Table 1. It was found that the band gap of doped samples decreases with increasing dopant content. The redshift of band gap in doped samples can be attributed to the sp-d exchange interactions between the band electrons and the localized d electrons of the Co^{2+} ions substituting Sn^{4+} ions [8, 28, 29]. Fang et al. [30] in their work reported that redshift in the band gap of Fe^{3+}-doped SnO_2 nanoparticles is due to the charge–transfer transition between the Fe^{3+} d-electrons and the SnO_2 conduction or valence band. Similar
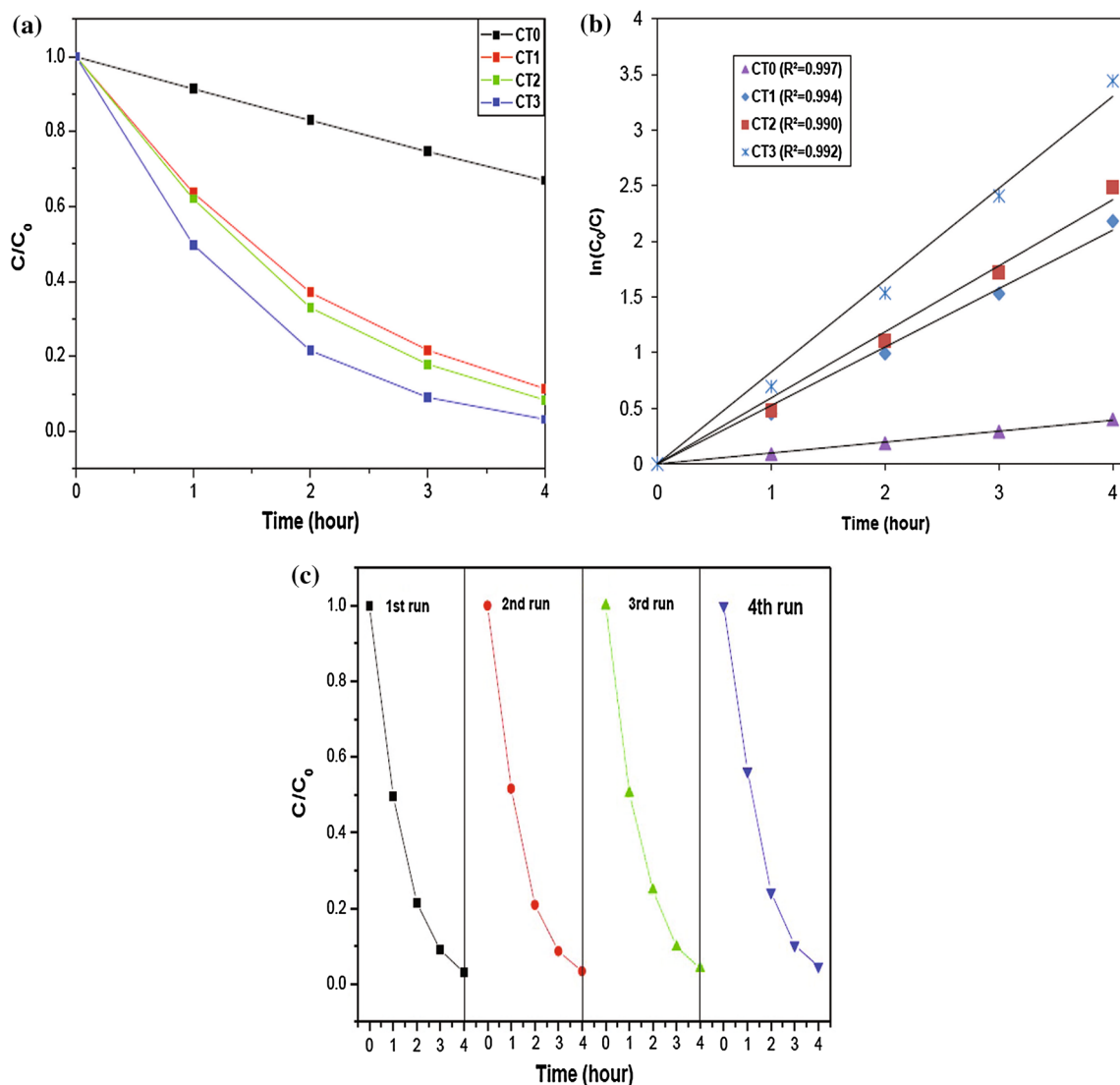
Fig. 8 a Effect of Co-doping concentration on the degradation of MB solution under sunlight exposure, **b** Kinetic fit for the degradation of MB with pure and Co-doped SnO$_2$ nanoparticles, **c** Stability test for sample CT3 for four runs

shift in the band gap has been reported in cobalt- and other transition metal ion-doped semiconductor materials [28, 31–34]. The lowering of band gap clearly indicates the incorporation of cobalt ions in SnO$_2$ crystal lattice. This would have played an important role for the enhancement of photocatalytic activity in doped samples as the defect levels formed act as charge carrier trapping site and minimize the electron–hole recombination.

4.2 Photocatalytic studies

Figure 7 shows the photocatalytic activity of sample CT3 evaluated by the degradation of MB at different time intervals of sunlight exposure. The decrease in the intensity
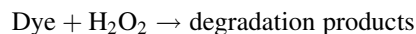
of absorption peak at 665 nm with time of exposure in sunlight clearly indicates the degradation of dye.

A basic mechanism of photocatalytic reaction can be explained as follows. When a photocatalyst is irradiated with light having energy equal to or greater than its band gap energy ($hv \geq E_{gb}$), then electrons migrate from valence band (VB) to conduction band (CB), and holes are formed in VB. The photogenerated holes and electrons then undergo oxidation and reduction process with water and dissolved oxygen, which results in the generation of reactive oxygen species such as hydroxyl radicals (·OH) and superoxide radical anions (·O$_2^-$). The superoxide radical anions thus obtained reacted with H$^+$ producing (HO$_2$) radicals, which upon subsequent collision with electrons produce hydrogen peroxide anions (HO$_2^-$). They then react
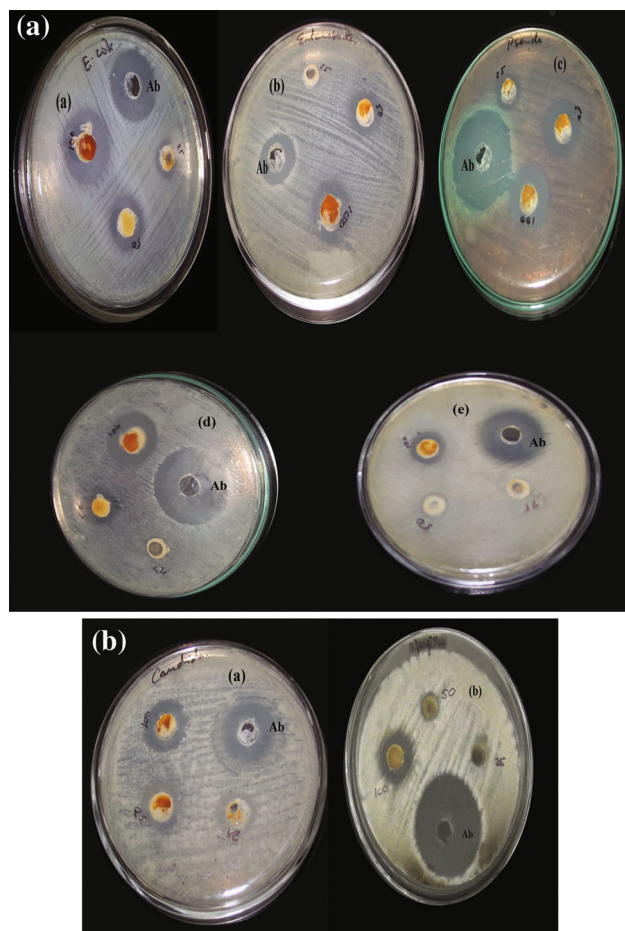
Fig. 9 a Antibacterial activity of sample CT3 against (*a*) *E. Coli* (*b*) *Enterobacter* spp., (*c*) *Pseudomonas aeruginosa*, (*d*) *Enterococcus faecalis*, and (*e*) *Staphylococcus aureus*. **b** Antifungal activity of sample CT3 against (*a*) *Candida Albicans* and (*b*) *Aspergillus niger*

with hydrogen ions to produce molecules of hydrogen per oxide (H_2O_2). The overall mechanism of photocatalytic degradation of dye can be represented by the following equations:

$$SnO_2 + hv \rightarrow h^+_{(VB)} + \bar{e}_{(CB)}$$

$$h^+_{(VB)} + H_2O \rightarrow \cdot OH + H^+$$

$$\bar{e}_{(CB)} + O_2 \rightarrow \cdot O_2^-$$

$$\cdot O_2^- + H^+ \rightarrow HO_2^{\cdot}$$

$$HO_2^{\cdot} + H^+ \rightarrow H_2O_2$$

$$Dye + \cdot OH \rightarrow degradation\ products$$

$$Dye + \cdot O_2^- \rightarrow degradation\ products$$

$$Dye + H_2O_2 \rightarrow degradation\ products$$
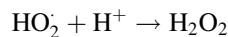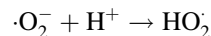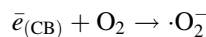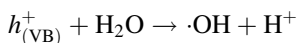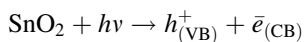
Several studies in the field of electrocatalysis of rutile-type oxides also report the role of similar hydroxo, oxo, or peroxo intermediate species in the enhancement of oxygen evolution reactions in those oxides [35–37]. Figure 8a presents the effect of Co-doping concentration on the degradation of MB. It can be found that the degradation of dye is faster in sample CT3, and about 97 % of the dye was degraded within 4 h under sunlight exposure. It is evident from UV spectra that the incorporation of Co^{2+} ions into SnO_2 matrix introduces new defect levels in the band gap of SnO_2, which can act as trap centers and thereby minimizes the recombination rate by the effective separation of electron–hole pairs. Moreover, the larger surface area of doped samples provides more photocatalytic reaction centers for adsorbing a large number of dye molecules, causing the degradation of dye effectively [38–40]. Wang et al. [38] and Stengl et al. [41] reported that large surface area and the presence of mesoporosity enhances the photocatalytic activity.

Figure 8b shows the plot of $\ln\left(C_0/C\right)$ versus time. The linear relationship of the plot indicates that the photodegradation of the dye obeys pseudo-first-order kinetics, and the rate expression is given by the equation [42–44],

$$\ln\left(C_0/C\right) = kt$$

where k is the pseudo-first-order rate constant, C_0 and C are the concentration at time $t = 0$ and t, respectively. The pseudo-first-order rate constants (k) of all the photocatalysts obtained from the plot of $\ln\left(C_0/C\right)$ with time are given in Table 1. The rate constants obtained clearly

Table 2 Antibacterial activity of pure and Co-doped SnO_2 nanoparticles at different concentrations (25, 50, 100 μg/ml)

Diameter of zone of inhibition (mm) for different concentrations (μg/ml)

Samples	*E. Coli*			*Enterobacter* spp.,			*Pseudomonas aeruginosa*			*Enterococcus faecalis*			*Staphylococcus aureus*		
	25	50	100	25	50	100	25	50	100	25	50	100	25	50	100
CT0	–	–	10	–	–	–	–	–	–	–	–	–	–	–	–
CT1	–	–	11	–	–	13	–	–	14	–	–	–	–	–	12
CT2	–	12	14	–	13	16	–	11	16	–	10	15	–	–	14
CT3	15	20	28	–	20	24	10	16	20	–	20	26	–	–	19
Gentamicin		30			28			34			32			30	

Table 3 Antifungal activity of pure and Co-doped SnO$_2$ nanoparticles at different concentrations (25, 50, 100 μg/ml)

Samples	Diameter of zone of inhibition (mm) for different concentrations (μg/ml)					
	Candida albicans			*Aspergillus niger*		
	25	50	100	25	50	100
CT0	–	–	12	–	–	–
CT1	–	11	14	–	–	–
CT2	–	12	15	–	9	15
CT3	13	19	21	–	11	21
Clotrimazole		24			30	

indicate that the photocatalytic activity of sample CT3 had a faster dye degradation of 8.4 times than the undoped sample.

The stability tests of the photocatalytic activity of sample CT3 for four runs are shown in Fig. 8c. The results clearly indicated that the photocatalyst was stable even after four runs without any significant loss of photocatalytic activity, showing its efficiency for the degradation of organic pollutants.

4.3 Antimicrobial activity

Figure 9a shows the results of antibacterial study of sample CT3 against 2 Gram-positive bacteria (*E. faecalis*, *S. aureus*) and 3 Gram-negative bacteria (*E. coli*, *Enterobacter* spp., *P. aeruginosa*) for three different concentrations, and Fig. 9b shows its antifungal results with *Candida albicans* and *Aspergillus niger*. The results of the antimicrobial studies of all the samples are summarized in Tables 2 and 3.

It was found that the diameter of the ZOI increased with increase in cobalt-doping percentage and also with the sample concentrations, and sample CT3 exhibits marked antimicrobial activity as compared to sample CT0. According to many published reports, several mechanisms have been proposed for the antimicrobial activity such as the generation of hydrogen per oxide H$_2$O$_2$ [reactive oxygen species (ROS)], large surface area/small particle size of the nanoparticles, and efflux mechanisms leading to the release of constituent ions [45–49]. From the photocatalytic studies, it was found that Co-doped SnO$_2$ nanoparticles were photocatalytic under visible light irradiation and could degrade the dye very effectively by ROS as explained in the mechanism of photocatalysis. The higher antibacterial activity of smaller nanoparticles is due to the generation of H$_2$O$_2$ which strongly depends on the surface area of the nanoparticles; larger the surface area, the more antibacterial activity [50]. Jalal et al. [51] studied the concentration-dependent antibacterial activity of ZnO nanofluids and found that the antibacterial activity increased with increasing nanofluid concentration and time, which is due to the increase in H$_2$O$_2$ concentration generated from the surface of ZnO. Furthermore, the binding of nanoparticles to the microbe surface by direct or electrostatic forces can also be bactericidal [52, 53]. Many studies have showed that even under ordinary room light, ROS generation could be possible from metal oxide nanoparticle suspensions, and the amount of ROS can be increased significantly when irradiated with visible light or with UV light, which in turn enhances the antimicrobial activity of the nanoparticles [11, 54, 55]. The antimicrobial activity of SnO$_2$ nanoparticles also depends on their band gap energy; lower band gap energy and higher surface area results in more bacteria adsorption and more facility of catalytic activity even under dark conditions [56]. In the present study, the antimicrobial tests were performed under laboratory light conditions and found remarkable enhancement in the antimicrobial activity of Co-doped samples which is due to the large surface area and small particle size, lower band gap energy of the nanoparticles, and the production of ROS, especially H$_2$O$_2$ on the surface of the nanoparticles that can penetrate the cell membrane and can cause damage to DNA and cellular proteins, leading to cell death.

5 Conclusions

Pure and Co-doped tin oxide nanoparticles were successfully synthesized by sol–gel method. The UV–Vis absorption spectra showed redshift in the absorption edge of doped samples, which enhances their absorption toward the visible light region. Compared to pure SnO$_2$, the doped samples exhibit an extra peak between 375 and 505 nm which can be related to the *d–d* electronic transition of Co^{2+} in SnO$_2$ lattice. The photocatalytic efficiency of pure and doped samples was determined by the degradation of MB solution under daylight illumination. It was found that the photocatalytic activity of SnO$_2$ is significantly enhanced by Co-doping because the incorporation of Co^{2+} ions into SnO$_2$ matrix introduces new defect levels in the band gap of SnO$_2$, which can act as trap centers and thereby minimize the recombination rate by the effective separation of electron–hole pairs. The antimicrobial studies

investigated against standard bacterial and fungal strains showed enhanced antimicrobial activity in doped samples, which is due to the large surface area and small particle size, lower band gap energy of the nanoparticles, and the production of ROS, especially H_2O_2 on the surface of the nanoparticles that can penetrate the cell membrane and can cause damage to DNA and cellular proteins, leading to cell death. Thus, the present study clearly indicates that Co-doped SnO_2 nanoparticles can be used as an excellent photocatalyst for the treatment of industrial waste water containing dye effluents and also as antimicrobial agents in consumer and industrial products.

References

1. Tischner A, Maier T, Stepper C, Kock A (2008) Ultrathin SnO_2 gas sensors fabricated by spray pyrolysis for the detection of humidity and carbon monoxide. Sens Actuators B Chem 134(2):796–802

2. Mohamed SH (2012) SnO_2 dendrites-nanowires for optoelectronic and gas sensing applications. J Alloy Compd 510(1):119–124

3. Ko YD, Kang JG, Park JG, Lee S, Kim DW (2009) Self-supported SnO_2 nanowire electrodes for high-power lithium-ion batteries. Nanotechnology 20:455701

4. Casados DS, Santiago EV, Lopez SH, Lopez MAC (2009) Characterization and photocatalytic performance of tin oxide. Ind Eng Chem Res 48(3):1249–1252

5. Singh AK, Nakate UT (2013) Microwave synthesis, characterization and photocatalytic properties of SnO_2 nanoparticles. Adv Nanoparticles 2:66–70

6. Duong TT, Choi HJ, He QJ, Le AT, Yoon SG (2013) Enhancing the efficiency of dye sensitized solar cells with an SnO_2 blocking layer grown by nanocluster deposition. J Alloy Compd 561:206–210

7. Etre AYE, Reda SM (2010) Characterisation of nanocrystalline SnO_2 thin film fabricated by electrodeposition method for dye-sensitized solar cell application. Appl Surf Sci 256:6601–6606

8. Entradas T, Cabrita JF, Dalui S, Nunes MR, Monteiro OC, Silvestre AJ (2014) Synthesis of sub-5 nm Co-doped SnO_2 nanoparticles and their structural, microstructural, optical and photocatalytic properties. Mater Chem Phys 147(3):563–571

9. Rashad MM, Ismail AA, Osama I, Ibrahim IA, Kandil AHT (2014) Decomposition of methylene blue on transition metals doped SnO_2 nanoparticles. CLEAN Soil Air Water 42(5):657–663

10. Rekha K, Nirmala M, Nair MG, Anukaliani A (2010) Structural, optical, photocatalytical and antibacterial activity of zinc oxide and manganese doped zinc oxide nanoparticles. Phys B Condens Matter 405(15):3180–3185

11. Yu B, Leung KM, Guo Q, Lau WM, Yang J (2011) Synthesis of Ag–TiO$_2$ composite nano thin film for antimicrobial application. Nanotechnology 22(11):115603

12. Nair MG, Nirmala M, Rekha K, Anukaliani A (2011) Structural, optical, photo catalytic and antibacterial activity of ZnO and Co doped ZnO nanoparticles. Mater Lett 65(12):1797–1800

13. Gupta K, Singh RP, Pandey A, Pandey A (2013) Photocatalytic antibacterial performance of TiO_2 and Ag-doped TiO_2 against *S. aureus*, *P. aeruginosa* and *E. coli*. Beilst J Nanotechnol 4:345–351

14. Shah AH, Manikandan E, Ahmed MB, Ganesan V (2013) Enhanced bioactivity of Ag/ZnO nanorods-A comparative antibacterial study. J Nanomed Nanotechnol 4(3):1–6

15. Zhang J, Gao L (2004) Synthesis and characterization of nanocrystalline tin oxide by sol–gel method. J Solid State Chem 177(4–5):1425–1430

16. Adnan R, Razana NA, Rahman IA, Farrukh MA (2010) Synthesis and characterization of high surface area tin oxide nanoparticles via the sol–gel method as a catalyst for the hydrogenation of styrene. J Chin Chem Soc 57(2):222–229

17. Fan C, Song X, Yin Z, Yu H, Sun S (2006) Preparation of SnO_2 hollow nanospheres by a solvothermal method. J Mater Sci 41:5696–5698

18. Niasari MS, Mir N, Davar F (2010) Synthesis, characterization and optical properties of tin oxide nanoclusters prepared from a novel precursor via thermal decomposition route. Inorganica Chimi Acta 363(8):1719–1726

19. Patil GE, Kajale DD, Gaikwad VB, Jain GH (2012) Preparation and characterization of SnO_2 nanoparticles by hydrothermal route. Intern Nano Lett 2:1–5

20. Cullity BD (1978) Elements of X-ray diffraction, 2nd edn. Addison-Wesely, Massachusetts

21. Azam A, Ahmed AS, Chaman M, Naqvi AH (2010) Investigation of electrical properties of Mn doped tin oxide nanoparticles using impedance spectroscopy. J Appl Phys 108:094329

22. Ahmed AS, Muhamed SM, Singla ML, Tabassum S, Naqvi AH, Azam A (2011) Band gap narrowing and fluorescence properties of nickel doped SnO_2 nanoparticles. J Lumin 131(1):1–6

23. Pillai SK, Sikhwivhilu LM, Hillie TK (2010) Synthesis, characterization and photoluminescence properties of Dy^{3+}-doped nano-crystalline SnO_2. Mater Chem Phys 120(2–3):619–624

24. Karthik K, Pandian SK, Jaya NV (2010) Effect of nickel doping on structural, optical and electrical properties of TiO_2 nanoparticles by sol–gel method. Appl Surf Sci 256(22):6829–6833

25. Krishnakumar T, Jayaprakash R, Pinna N, Phani AR, Passacantando M, Santucci S (2009) Structural, optical and electrical characterization of antimony-substituted tin oxide nanoparticles. J Phys Chem Solids 70(6):993–999

26. Morales AE, Mora ES, Pal U (2007) Use of diffuse reflectance spectroscopy for optical characterization of un-supported nanostructures. Rev Mex De Fis 53(5):18–22

27. Choudhury B, Choudhury A (2012) Luminescence characteristics of cobalt doped TiO_2 nanoparticles. J Lumin 132(1):178–184

28. Lima MK, Fernandes DM, Silva MF, Baesso ML, Neto AM, Morais GR, Nakamura CV, Caleare AO, Hechenleitner AAW, Pineda EAG (2014) Co-doped ZnO nanoparticles synthesized by an adapted sol–gel method: effects on the structural, optical, photocatalytic and antibacterial properties. J Sol-Gel Sci Technol 72:301–309

29. Kim DH, Hong HS, Kim SJ, Song JS, Lee KS (2004) Photocatalytic behaviours and structural characterization of nanocrystalline Fe-doped TiO_2 synthesized by mechanical alloying. J Alloy Compd 375(1–2):259–264

30. Fang LM, Zu XT, Li ZJ, Zhu S, Liu CM, Zhou WL, Wang LM (2008) Synthesis and characteristics of Fe^{3+}-doped SnO_2 nanoparticles via sol–gel-calcination or sol–gel-hydrothermal route. J Alloy Compd 454(1–2):261–267

31. Santara B, Pal B, Giri PK (2011) Signature of strong ferromagnetism and optical properties of Co doped TiO_2 nanoparticles. J App Phys 110:114322

32. He R, Hocking RK, Tsuzuki T (2012) Co-doped ZnO nanopowders: location of cobalt and reduction in photocatalytic activity. Mater Chem Phys 132(2–3):1035–1040

33. Djaja NF, Montja DA, Saleh R (2013) The effect of Co incorporation into ZnO nanoparticles. Adv Mater Phys Chem 3:33–41

34. Choudhury B, Dey M, Choudhury A (2013) Defect generation, d–d transition, and band gap reduction in Cu-doped TiO_2 nanoparticles. Int Nano Lett 3(1):1–8

35. Rossmeisl J, Qu ZW, Zhu H, Kroes GJ, Norskov JK (2007) Electrolysis of water on oxide surfaces. J Electroanal Chem 607:83–89

36. Man IC, Su HY, Vallejo FC, Hansen HA, Martinez JI, Inoglu NG, Kitchin J, Jaramillo TF, Norskov JK, Rossmeisl J (2011) Universality in oxygen evolution electrocatalysis on oxide surfaces. Chem Cat Chem 3:1159–1165

37. Petrykin V, Macounova K, Okube M, Mukerjee S, Krtil P (2013) Local structure of Co doped RuO_2 nanocrystalline electrocatalytic materials for chlorine and oxygen evolution. Catal Today 202:63–69

38. Wang QQ, Lin BZ, Xu BH, Li XL, Chen ZJ, Pian XT (2010) Preparation and photocatalytic properties of mesoporous SnO_2-hexaniobate layered nanocomposite. Microporous Mesoporous Mater 130(1–3):344–351

39. Foletto EL, Battiston S, Collazzo GC, Bassaco MM, Mazutti MA (2012) Degradation of leather dye using CeO_2–SnO_2 nanocomposite as photocatalyst under sunlight. Water Air Soil Pollut 223:5773–5779

40. Behnajady MA, Tohidi Y (2014) Synthesis, characterization and photocatalytic activity of Mg-impregnated ZnO–SnO_2 coupled nanoparticles. Photochem Photobiol 90(1):51–56

41. Stengl V, Bakardjieva S, Murafa N (2009) Preparation and photocatalytic activity of rare earth doped TiO_2 nanoparticles. Mater Chem Phys 114:217–226

42. Kuzhalosai V, Subash B, Senthilraja A, Dhatshanamurthi P, Shanthi M (2013) Synthesis, characterization and photocatalytic properties of SnO_2–ZnO composite under UV-A light. Spectrochim Acta A Mol Biomol Spectrosc 115:876–882

43. Bandekar G, Rajurkar NS, Mulla IS, Mulik UP, Amalnerkar DP, Adhyapak PV (2014) Synthesis, characterization and photocatalytic activity of PVP stabilized ZnO and modified ZnO nanostructures. Appl Nanosci 4:199–208

44. Haldorai Y, Shim JJ (2014) Novel chitosan-TiO_2 nanohybrid: preparation, characterization, antibacterial, and photocatalytic properties. Poly Compos 35(2):327–333

45. Sawai J, Shoji S, Igarashi H, Hashimoto A, Kokugan T, Shimizu M, Kojima H (1998) Hydrogen peroxide as an antibacterial factor in zinc oxide powder slurry. J Ferment Bioeng 86(5):521–522

46. Talebian N, Amininezhad SM, Doudi M (2013) Controllable synthesis of ZnO nanoparticles and their morphology-dependent antibacterial and optical properties. J Photochem Photobiol B Biol 120:66–73

47. Stankovic A, Dimitrijevic S, Uskokovic D (2013) Influence of size scale and morphology on antibacterial properties of ZnO powders hydrothemally synthesized using different surface stabilizing agents. Colloids Surf B Biointerfaces 102:21–28

48. Li Y, Zhang W, Niu J, Chen Y (2012) Mechanism of photogenerated reactive oxygen species and correlation with the antibacterial properties of engineered metal-oxide nanoparticles. ACS Nano 6(6):5164–5173

49. Suyana P, Kumar SN, Kumar BSD, Nair BN, Pillai SC, Mohamed AP, Warrier KGK, Hareesh US (2014) Antifungal properties of nanosized ZnS particles synthesised by sonochemical precipitation. RSC Adv 4(17):8439–8445

50. Padmavathy N, Vijayaraghavan R (2008) Enhanced bioactivity of ZnO nanoparticles-an antimicrobial study. Sci Technol Adv Mater 9:1–7

51. Jalal R, Goharshadi EK, Abareshi M, Moosavi M, Yousefi A, Nancarrow P (2010) ZnO nanofluids: green synthesis, characterization, and antibacterial activity. Mater Chem Phys 121:198–201

52. Stoimenov PK, Klinger RL, Marchin GL, Klabunde KJ (2002) Metal oxide nanoparticles as bactericidal agents. Langmuir 18(17):6679–6686

53. Xie Y, He Y, Irwin PL, Jin T, Shi X (2011) Antibacterial activity and mechanism of action of zinc oxide nanoparticles against campylobacter jejuni. Appl Environ Microbiol 77(7):2325–2331

54. Lipovsky A, Tzitrinovich Z, Friedmann H, Applerot G, Gedanken A, Lubart R (2009) EPR study of visible light-induced ROS generation by nanoparticles of ZnO. J Phys Chem C 113(36):15997–16001

55. Jones N, Ray B, Ranjit KT, Manna AC (2008) Antibacterial activity of ZnO nanoparticle suspensions on a broad spectrum of microorganisms. FEMS Microbiol Lett 279(1):71–76

56. Talebian N, Zavvare HSH (2014) Enhanced bactericidal action of SnO_2 nanostructures having different morphologies under visible light: influence of surfactant. J Photochem Photobiol B Biol 130:132–139